Solar Energy Materials & Solar Cells 310 (2027) 114802

Contents lists available at ScienceDirect

Solar Energy Materials and Solar Cells

journal homepage: www.elsevier.com/locate/solmat

Unveiling the layer-resolved mechanical landscape of multilayer hybrid perovskite solar cells by statistical nanoindentation

Miguel Ángel Garrido-Maneiro [a,*], María del Carmen López-González [b], Belén Arredondo [b], Beatriz Romero [b,c], Pedro Poza [a,c], Jesús Rodríguez [a,c]

[a] DIMME – Durability and Mechanical Integrity of Structural Materials, Escuela Superior de Ciencias Experimentales y Tecnología, Universidad Rey Juan Carlos, c/ Tulipán s/n, Móstoles, Madrid, 28933, Spain

[b] Área de Tecnología Electrónica, Escuela Superior de Ciencias Experimentales y Tecnología, Universidad Rey Juan Carlos, c/Tulipán s/n, Móstoles, Madrid, 28933, Spain

[c] ITPS – Instituto de Tecnologías para la Sostenibilidad (ITPS), Universidad Rey Juan Carlos, c/Tulipán s/n, Móstoles, Madrid, 28933, Spain

ARTICLE INFO

Keywords:
Hybrid perovskite solar cells
Statistical nanoindentation
Conditional deconvolution
Gaussian mixture model

ABSTRACT

Perovskite solar cells rely on complex multilayer architectures whose mechanical integrity is increasingly recognized as a critical factor for long-term operational stability. Despite extensive characterization of methylammonium lead iodide ($MAPbI_3$), the mechanical properties of emerging multi-cation perovskites within complete device stacks remain poorly understood. In this manuscript, we present a system-level mechanical characterization of two perovskite solar cell architectures using depth-resolved nanoindentation. By combining continuous stiffness measurements with statistical deconvolution, we isolate the elastic modulus and hardness of individual layers across the full device stack. The approach accurately reproduces reported values for common transport layers and $MAPbI_3$, demonstrating robustness. We further report, for the first time, the intrinsic mechanical properties of the four-cation perovskite $CsRbFAMAPb(IBr)_3$, which exhibits a similar elastic modulus but substantially higher hardness than $MAPbI_3$. These results reveal a higher resistance to localized indentation-induced plastic deformation in multi-cation absorbers and underscore the importance of mechanical characterization when designing next-generation perovskite solar cells.

1. Introduction

Perovskite solar cells (PSCs) have emerged as one of the most promising photovoltaic technologies of the past decade, due to their high-power conversion efficiency, low manufacturing cost, and design versatility. These cells generally have a multilayer structure [1]. Each layer fulfils a distinct electronic and functional role essential for achieving high power-conversion efficiency and operational stability. In their standard architecture, PSCs comprise a photoactive perovskite absorber layer, an electron transport layer, a hole transport layer, and charge-collecting electrodes, a configuration that enables efficient light absorption, charge separation, and selective carrier extraction. Reviews [2] in the field emphasize that interfacial phenomena largely dictate device performance, making the incorporation of dedicated transport layers and engineered interfaces critical for reducing non-radiative recombination, optimizing band alignment, and improving long-term stability under operational stressors. Consequently, the multilayer design is not merely structural but a functional necessity that allows PSCs to simultaneously maximize optoelectronic efficiency and maintain mechanical and environmental robustness [3,4].

The integration of perovskite layers into photovoltaic cells offers significant advantages in terms of both performance and durability, particularly when considering the mechanical and environmental challenges these devices face during their operational lifetime. An ideal photovoltaic material must exhibit high power conversion efficiency, long-term stability, mechanical robustness, and compatibility with scalable manufacturing processes. Perovskites, especially those based on hybrid organic-inorganic halide compositions, fulfil many of these criteria due to their tuneable bandgap, high absorption coefficients, and long carrier diffusion lengths [5,6]. However, during service, solar cells are subjected to various forms of mechanical and environmental stress, including thermal cycling, humidity, UV exposure, and mechanical loading, which can lead to degradation phenomena such as delamination, cracking, fatigue, and erosion [7]. These failure modes are often

* Corresponding author.
E-mail address: miguelangel.garrido@urjc.es (M.Á. Garrido-Maneiro).

https://doi.org/10.1016/j.solmat.2026.114802
Received 16 June 2026; Received in revised form 13 October 2026; Accepted 23 October 2026
Available online 27 October 2026
0927-0248/© 2026 The Authors. Published by Elsevier B.V. This is an open access article under the CC BY-NC-ND license (http://creativecommons.org/licenses/by-nc-nd/4.0/).

exacerbated by residual stresses within the thin films, ion migration, and the presence of structural defects [8]. Therefore, the mechanical properties of the perovskite layer, such as elastic modulus and hardness, play a crucial role in determining the device's performance and may provide valuable information regarding its response to these degradation phenomena. Incorporating mechanically optimized perovskite compositions could enhance the overall reliability and lifespan of the device. Moreover, the ability to fabricate perovskite layers via low-temperature, solution-based processes enables the development of flexible and lightweight solar modules, expanding their applicability to portable and wearable technologies [9,10]. Thus, understanding and improving the mechanical behaviour of perovskite materials is essential for advancing the commercial viability of next-generation photovoltaic systems.

Among the most extensively studied formulations is methylammonium lead iodide ($MAPbI_3$ or MAPI), which has been widely used as a benchmark absorber material. $MAPbI_3$-based solar cells have demonstrated power conversion efficiencies exceeding 20% under laboratory conditions. More recently, other optimized perovskite compositions have achieved efficiencies above 26% [11]. These high efficiencies are attributed to $MAPbI_3$'s favourable optoelectronic properties, including a direct bandgap of approximately 1.53 eV, high absorption coefficients in the visible spectrum, long carrier diffusion lengths, and low exciton binding energy [12,13]. Structurally, $MAPbI_3$ crystallizes in a tetragonal phase at room temperature, which contributes to its efficient charge transport and light-harvesting capabilities. Additionally, its compatibility with low-temperature solution processing makes it attractive for scalable and cost-effective manufacturing. Despite its mechanical softness, $MAPbI_3$ has been shown to form uniform, pinhole-free films that are essential for device performance. These characteristics have made $MAPbI_3$ a benchmark material in perovskite solar cell research and a reference point for evaluating the performance of newer, more complex perovskite compositions.

From a mechanical standpoint, $MAPbI_3$ exhibits properties that, while suitable for device fabrication, its mechanical fragility, characterized by a low Young's modulus, hardness, and fracture toughness, poses significant challenges for the long-term reliability and durability of PSCs under operational and environmental stresses [14]. Previous studies have reported that the elastic modulus of $MAPbI_3$ ranges from 10 to 28 GPa, while its hardness varies between 0.3 and 0.6 GPa, depending on synthesis conditions and characterization methods [15–17]. These values reflect a relatively soft and ductile nature, which may facilitate the formation of microcracks or plastic deformations under prolonged operational conditions, especially in environments with thermal or mechanical fluctuations [15].

Understanding the mechanical properties of these materials used in solar cells is essential for predicting their behaviour under mechanical, thermal, or environmental stress. Throughout the operational lifetime of a photovoltaic device, the active layers are subjected to thermal cycling, vibrations, impacts, and other factors that can induce deformation, delamination, or structural failure. Therefore, accurate mechanical characterization not only enables optimization of device design but also helps anticipate potential failure mechanisms and improve long-term durability [17].

In this way, several comprehensive reviews have addressed the mechanical and environmental stability of perovskite-based devices. Baumann et al. provided an extensive overview of degradation mechanisms in perovskite solar cells, highlighting the role of mobile ions, moisture, and thermal cycling in mechanical failure [18]. They emphasize that mechanical stress, both intrinsic (e.g., thermal expansion mismatch) and extrinsic (e.g., encapsulation pressure), can lead to delamination, cracking, and phase segregation, ultimately compromising device performance. Kumar et al. [19] highlighted that although perovskite solar cells achieve high power conversion efficiencies, their practical implementation was limited by issues such as lead toxicity and material instability under environmental stress. In that research, they developed lead-free and more stable perovskite materials, as well as improved processing strategies to enhance durability and environmental compatibility.

Mechanical characterization of these materials has been primarily conducted using nanoindentation testing, a technique that enables precise measurement of elastic modulus and hardness at the nanoscale [20]. This method would be particularly useful in multilayer systems such as solar cells, where the mechanical properties of each layer can significantly influence the overall behaviour of the device. In the case of $MAPbI_3$, nanoindentation studies have helped correlate the material's microstructure with its mechanical response, revealing the influence of factors such as grain size, crystallographic orientation, and structural defects. These factors contribute to the broad ranges of elastic modulus and hardness values reported in the literature by different authors [16,21]. Despite the progress made with $MAPbI_3$, this material suffers from thermal and environmental stability issues that limit its long-term commercial viability. Therefore, if the commercial viability of these coatings is to be expanded, it is essential to understand and characterize the impact that environmental and operating conditions have on their performance. This requires analysing not only their optoelectronic behaviour but also their mechanical integrity. Both properties govern the functional performance of solar cells, which, as outlined in the introduction, ultimately depends on the integrated response of the entire multilayer architecture. However, conventional nanoindentation studies have largely characterized the perovskite layer in isolation, neglecting the mechanical contributions of the remaining layers within the device stack. Accordingly, advanced nanoindentation approaches are required to assess the mechanical properties of solar cells at the full system level, capturing not only the perovskite layer but also the additional functional layers and the underlying substrate.

Recent efforts have focused on enhancing the mechanical and environmental stability of PSCs through compositional engineering, including the development of multi-cation perovskites. New formulations of quaternary or quasi-quaternary perovskites have been developed. These materials, incorporating combinations formamidinium (FA^+), cesium (Cs^+), methylammonium (MA^+), and rubidium (Rb^+), such as $CsRbFAMAPb(IBr)_3$, which incorporates a mixture of organic and inorganic cations (formamidinium, methylammonium, cesium, and rubidium) and a combination of halides (iodide and bromide). This composition has shown significant improvements in thermal stability, moisture resistance, and defect tolerance, while maintaining high photovoltaic efficiency [22]. The inclusion of inorganic cations such as Cs^+ and Rb^+ in the crystal lattice contributes to greater structural stability, while the partial substitution of I^- with Br^- allows for bandgap tuning, optimizing spectral absorption.

However, despite these optoelectronic and chemical advantages, the mechanical properties of this new generation of perovskites remain largely unexplored. A few studies have been done concerning the effect of the incorporation of multi-cations on the mechanical performance. Afre and Pugliese [23] discussed the mechanical stability of flexible PSCs, noting that the integration of multi-cation compositions and novel encapsulation strategies can significantly improve mechanical resilience. Their review underscores the importance of optimizing both the perovskite composition and the device architecture to mitigate mechanical degradation under bending, stretching, and environmental exposure. In addition, experimental studies have shown that multi-cation perovskites exhibit superior mechanical properties compared to single-cation counterparts. For instance, perovskites incorporating FA^+ and Cs^+ tend to form more robust crystal lattices, which enhance fracture resistance and reduce defect propagation [24].

Even though, the lack of information on the effect of these perovskites, based on multi-cation additions, on the elastic modulus and hardness represents a barrier to fully assessing their reliability under real-world operating conditions.

In this context, while the mechanical properties of $MAPbI_3$ are well documented, the same cannot be said for the $CsRbFAMAPb(IBr)_3$ perovskite. The absence of data on its elastic modulus and hardness

prevents a direct comparison with traditional systems and limits the ability to predict its in-service behaviour. For this reason, the objective of the present work was to experimentally determine the mechanical properties of multilayer structures composed of a MAPI layer and a four-cation $CsRbFAMAPb(IBr)_3$ perovskite layer. More precisely, nanoindentation tests were conducted to obtain the elastic modulus and hardness of each layer comprising two proposed solar-cell architectures, providing insights into the interplay between composition, structure, and mechanical performance in hybrid perovskite systems. Our findings contribute to the broader understanding of the layer-resolved mechanical response of perovskite-based devices, a factor increasingly recognized as critical for their commercial viability. To this end, different nanoindentation methodologies were combined to achieve this goal; namely, continuous stiffness measurement (CSM) and statistical nanoindentation.

2. Materials and methods

2.1. Materials: Multilayer architectures of perovskite solar cells

PSCs involve a multilayer architecture designed to optimize light absorption, charge separation, and charge transport. Two different types of cells were manufactured. Both device types described Type 1 ($MAPbI_3$-based) and Type 2 ($CsRbFAMAPb(IBr)_3$-based), share a common substrate and electron transport layer (ETL) configuration, differing primarily in the composition and thickness of the perovskite absorber layer.

The fabrication of PSCs involves Patterned fluorine-doped tin oxide (FTO) coated glass substrates (sheet resistance: 12–14 Ω/sq) were used for the deposition of electron transport layer (ETL) and perovskite absorber layers. Prior to use, the substrates were brushed with a 2% v/v aqueous Hellmanex solution, followed by thorough rinsing with deionized water. They were then sequentially cleaned in consecutive ultrasonic baths with Hellmanex solution, deionized water, isopropanol, and acetone, each for 15 min. After drying with a nitrogen stream, the substrates were treated with UV-ozone for 15 min using an ozone cleaner.

Following the cleaning procedure, a compact dioxide layer (c-TiO_2) was deposited by spray pyrolysis at 450 °C using a precursor solution of titanium diisopropoxide bis(acetylacetonate) dissolved in absolute ethanol. Oxygen was used as the carrier gas. After deposition, the substrates were kept at 450 °C for 30 min to ensure complete crystallization and then cooled to room temperature. The mesoporous TiO_2 layer (m-TiO_2) was prepared by diluting a commercial TiO_2 paste (Sigma-Aldrich, 18NRT) in absolute ethanol. This suspension was deposited onto the compact layer by spin coating 100 μL at 4000 rpm for 10 s with a ramp of 2000 rpm/s. The films were immediately dried at 125 ∘C for 10 min and then annealed at 450 ∘C using a gradual temperature ramp. Together, the c-TiO_2 and m-TiO_2 layers constitute ETL.

Two different perovskite compositions were prepared: $MAPbI_3$ and the quadruple-cation mixed-halide perovskite $CsRbFAMAPb(IBr)_3$. All precursor preparation and film deposition steps were carried out inside a nitrogen-filled glovebox (O_2 and $H_2O < 1$ ppm) to prevent degradation due to moisture or oxygen exposure.

The $MAPbI_3$ precursor solution was prepared by dissolving lead iodide (PbI_2, 1 M, Sigma-Aldrich) in a 9:1 v/v mixture of DMF and DMSO, heated to 65–70 °C until fully dissolved. After cooling to room temperature, the solution was added to a pre-weighed amount of methylammonium iodide (MAI, Ossila) to obtain the final perovskite precursor. For deposition, 50 μL of the solution were spin-coated onto the substrate at 4000 rpm for 50 s. After 8 s of spinning, 500 μL of chlorobenzene were dropped as an antisolvent. The films were then annealed at 100 °C for 10 min to facilitate crystallization and solvent removal.

The $CsRbFAMAPb(IBr)_3$ perovskite precursor was prepared using four inorganic stock solutions and two organic halide salts. Stock solutions included: 1.5 M PbI_2 (TCI) and 1.5 M $PbBr_2$ (TCI) in DMF:DMSO (4:1 v/v), 1.5 M CsI (ABCR) in DMSO, and 1.5 M RbI (ABCR) in DMF: DMSO (4:1 v/v). These solutions were heated to 80 °C until fully dissolved and then cooled to room temperature before use. Separately, formamidinium iodide (FAI) and methylammonium bromide (MABr) (Greatcell Solar) were weighed and dissolved in the respective PbI_2 and $PbBr_2$ stock solutions to form $FAPbI_3$ and $MAPbBr_3$ precursors. These were combined in a 5:1 v/v ratio to obtain the $FAMAPb(IBr)_3$ solution. Finally, 5% v/v of CsI and 5% v/v of RbI stock solutions were added to produce the final $CsRbFAMAPb(IBr)_3$ formulation. For deposition, 80 μL of the solution were spin-coated using a two-step program: 1000 rpm for 10 s followed by 6000 rpm for 20 s. During the second step, 200 μL of chlorobenzene were dropped onto the spinning substrate 5 s before the end. The films were annealed at 100 °C for 60 min to complete the crystallization. The resulting nominal composition of this perovskite was $Cs_{0.05}Rb_{0.05}(FA_{0.83}MA_{0.17})_{0.9}Pb(I_{0.83}Br_{0.17})_3$.

Fig. 1 shows a comparison between the absorption spectra of $MAPbI_3$ and $CsRbFAMAPb(IBr)_3$ thin films. Both layers were prepared under the same conditions. As can be seen, there is a notable increase in absorption for the $CsRbFAMAPb(IBr)_3$ perovskite, with values approaching 100% across a broad range of the visible spectrum. This increase in absorption results in greater charge generation, leading to an increase in the extracted current and, ultimately, in the Power Conversion Efficiency (PCE).

Table 1 shows a summary of the layer structure composition of both cells' types including the thickness of each layer. This information was obtained from the images captured from the cross-sections of the devices using a high-resolution Nova Nano SEM230 field emission gun scanning electron microscope (SEM) (see Fig. 2a) and following the methodology reported in previous works [25]. Both cells are composed of five layers, including the glass substrate.

A comparison between $MAPbI_3$ and $CsRbFAMAPb(IBr)_3$ solar cells reveals clear differences in power-conversion efficiency (PCE) that arise from their distinct compositions and resulting microstructures. Standard $MAPbI_3$ devices typically exhibit efficiencies around 15%, but suffer from pronounced ionic migration, low activation energies for iodide diffusion (0.29–0.38 eV), and structural instabilities that lead to accelerated performance losses under thermal stress [26–28]. In contrast, the mixed-cation mixed-halide $CsRbFAMAPb(IBr)_3$ architecture studied here achieves higher efficiency and demonstrates markedly enhanced thermal and operational stability owing to its quadruple-cation formulation. Fig. 2b shows the J-V characteristics of the champion devices measured under AM1.5G illumination, while the inset table summarizes the average photovoltaic parameters obtained from a batch of 32 fabricated solar cells. The $MAPbI_3$ devices exhibited an average J_{SC} of

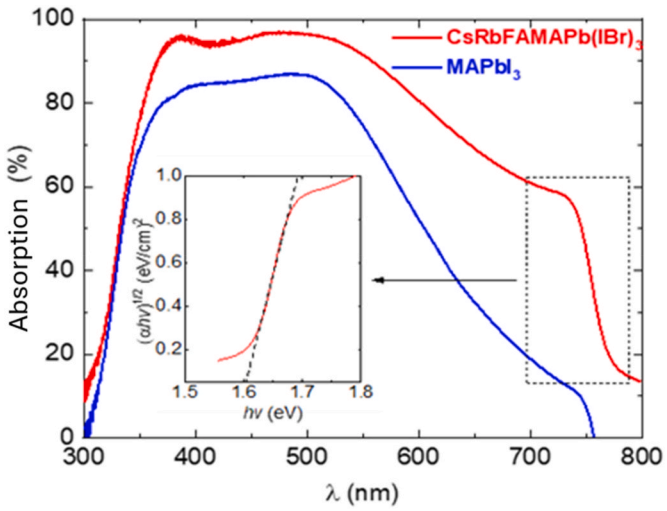


Fig. 1. Absorption spectra of $CsRbFAMAPb(IBr)_3$ and $MAPbI_3$. Inset shows the E_G ~1.6 eV extracted from the T_{auc} plot for the $CsRbFAMAPb(IBr)_3$ perovskite.

Table 1
Multilayer structure of the solar cells.

Material	Layer composition	Thickness (nm)
Solar cell: Type 1	Substrate: Glass + commercial FTO	400-450 (FTO layer)
	TiO_2 compact layer (c-TiO_2)	40-60
	TiO_2 mesoporous layer (m-TiO_2)	180
	$MAPbI_3$ perovskite	595
Solar cell: Type 2	Substrate: Glass + commercial FTO	400-450 (FTO layer)
	TiO_2 compact layer (c-TiO_2)	40-60
	TiO_2 mesoporous layer (m-TiO_2)	180
	$CsRbMAFAPb(IBr)_3$ perovskite	644

18.43 ± 0.22 mA cm^{-2}, a V_{OC} of 1.06 ± 0.02 V, an FF of 0.72 ± 0.03, and a PCE of $14.02 \pm 0.47\%$. In comparison, the $CsRbFAMAPb(IBr)_3$ devices showed a slightly lower J_{SC} of 17.58 ± 0.35 mA cm^{-2} but higher V_{OC} and FF values of 1.09 ± 0.02 V and 0.75 ± 0.03, respectively, resulting in an improved average PCE of $14.50 \pm 0.65\%$. These results indicate that the incorporation of the mixed-cation/mixed-halide composition enhances device performance primarily through gains in open-circuit voltage and fill factor, which compensate for the modest reduction in photocurrent density.

Additionally, the incorporation of Cs^+, Rb^+, FA^+, and MA^+ produces a more constrained and structurally robust perovskite lattice with larger grains, reduced defect density, and a significantly higher iodide ion activation energy of 0.63 ± 0.08 eV, which suppresses ion migration by several orders of magnitude compared to $MAPbI_3$ (diffusion coefficient $\approx 10^{-14}$ cm^2/s vs. 10^{-9} cm^2/s). These microstructural improvements mitigate interfacial and bulk recombination, stabilize the α-phase, and reduce hysteresis, collectively enabling $CsRbFAMAPb(IBr)_3$ devices to maintain efficiency more effectively across temperature variations than their $MAPbI_3$ counterparts [25].

2.2. Methods: Depth-resolved mechanical analysis by nanoindentation tests

Depth sensing indentation, commonly referred to as nanoindentation, is a high-precision mechanical testing technique used to determine the mechanical properties of materials at small scales, particularly hardness and elastic modulus. The method involves pressing a sharp indenter of known geometry, typically made of diamond, into the surface of a material while continuously recording the applied load and the corresponding penetration depth. This process is carried out through a controlled loading and unloading cycle, during which a force–displacement curve is generated. The shape and characteristics of this curve provide critical information about the material's response to deformation. One of the most widely adopted analytical approaches for interpreting nanoindentation data is the Oliver and Pharr method [29]. This method focuses on the unloading portion of the force–displacement curve and providing the values of elastic modulus, E, and hardness, H, of the indented material [30].

The accuracy and reliability of the mechanical properties obtained through nanoindentation depend heavily on the precise calibration of the indenter tip geometry. This calibration is essential because any deviation or wear in the tip shape can lead to significant errors in the calculated contact area and, consequently, in the derived mechanical properties. To ensure consistency and accuracy, calibration is typically performed using a reference material with well-known mechanical properties, such as fused silica, which offers a stable and reproducible response under indentation.

In this work a combination of continuous stiffness measurement methodology (CSM) and statistical nanoindentation was used. The CSM technique is an advanced method used in nanoindentation to continuously measure the contact stiffness of a material as a function of penetration depth during a single indentation cycle. Unlike traditional quasi-static indentation, where stiffness is derived only from the unloading segment, CSM superimposes a small oscillatory force onto the primary loading signal throughout the indentation process. This dynamic excitation allows for real-time measurement of stiffness at each depth increment, enabling the calculation of depth-dependent mechanical properties such as hardness and elastic modulus. The method is particularly advantageous for characterizing thin films or graded materials, as it provides a continuous profile of mechanical behaviour rather than a single averaged value. The stiffness is extracted from the phase and amplitude response of the material to the oscillatory load, and this information is used in conjunction with the Oliver and Pharr framework to compute mechanical properties at each depth [31,32].

Statistical nanoindentation is a high-throughput mechanical characterization methodology in which large arrays of closely spaced indents, often numbering in the hundreds or thousands, are performed to capture the mechanical heterogeneity of a material with robust statistical significance. Unlike conventional single-point indentation, statistical nanoindentation emphasizes spatial sampling density to resolve distributions of hardness and elastic modulus associated with distinct microstructural features, phases, or defect populations. This approach inherently accounts for microstructural variability, enabling to identify mechanically distinct domains through probabilistic methods. For example, in previous work, Ulm and co-workers established the statistical nanoindentation technique as a powerful method for characterizing

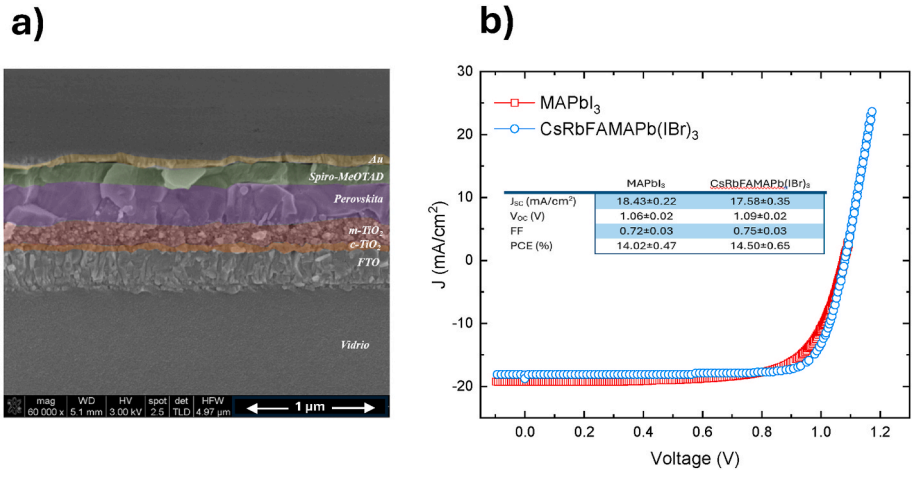


Fig. 2. a) Cross-sectional SEM image of the Glass/FTO/c-TiO_2/m-TiO_2/$CsRbFAMAPb(IBr)_3$/Spiro-OMeTAD/Au device; b) J-V curves of both devices including a table with the average values and the corresponding standard deviations of Open Circuit Voltage (V_{OC}), Short Circuit Current Density (J_{SC}), Fill Factor (FF) and Power Conversion Efficiency (PCE).

hydrated nanocomposites such as cementitious C–S–H, bone mineral (apatite), and clay-based shales. This methodology relies on performing large grids of instrumented indentation tests on a single polished surface and analyzing the resulting load–displacement curves to extract statistically representative distributions of elastic modulus and hardness for the mechanically distinct phases present within the microstructure. By treating each shallow indentation as an independent mechanical sampling event and applying probabilistic deconvolution to the populations of modulus–hardness values obtained at the surface, the technique enables in-plane phase identification and quantification with high spatial resolution [33]. That is, unlike conventional statistical nanoindentation, where a probabilistic analysis is performed on elastic modulus and hardness values obtained from multiple indents made solely on the material surface to identify and characterize its microstructural constituents, in this work the analysis is instead conducted on depth-dependent data. By using the mechanical responses recorded throughout the indentation process, this approach enables layer-resolved evaluation of each constituent layer within the solar-cell stack.

Mechanical characterization was focused on the glass/FTO/c-TiO_2/m-TiO_2/perovskite multilayer stack, since these layers constitute the structural system that dominates the mechanical response of the device under indentation loading. The objective of the present work is the determination of the elastic modulus and hardness of the mechanically relevant constituents of the solar-cell architecture and, in particular, the characterization of the perovskite absorber layer. For this reason, the hole transport layer (HTL) and the top metallic electrode were not included in the analysis. Furthermore, since both device architectures share the same substrate and electron-transport-layer configuration, while differing mainly in the composition of the perovskite absorber, the selected stack allows the influence of the perovskite formulation on the mechanical response to be identified and quantified.

Nanoindentation tests were performed on one sample of type 1 and three samples of type 2, using a diamond Berkovich tip. The $MAPbI_3$ device analysed in this study was included primarily as a reference system to validate the nanoindentation and statistical deconvolution methodology. Since elastic modulus and hardness values for $MAPbI_3$ have been extensively reported in the literature, the objective was to verify that the mechanical populations extracted from the nanoindentation analysis were consistent with previously reported ranges. Conversely, because equivalent layer-specific mechanical-property data are not available for the multi-cation perovskite, three independently fabricated devices were characterised to assess both within-device and between-device variability and to obtain representative mechanical-property estimates. The geometry of the indenter was calibrated on amorphous silica by imposing a nominal elastic modulus of 72 GPa up to a maximum penetration depth of 3000 nm. Subsequently, indentation arrays were programmed on the glass substrate using this calibration. Prior to the indentations, the surface was cleaned with isopropanol to remove dust and dirt. A total of 80 indentations were carried out using the continuous stiffness measurement module (CSM), spaced 100 μm apart, with a maximum penetration depth of 1500 nm. A load–unload cycling frequency of 35 Hz was selected, with an oscillation amplitude of 2 nm, superimposed during the application of the main loading cycle. For each of the multiple cycles, the evolution of the elastic modulus and hardness as a function of penetration depth was determined. The elastic modulus calculations were carried out assuming a Poisson's ratio of 0.20 for all constituent layers.

Fig. 3a shows a typical force-displacement curve extracted from nanoindentation test carried out onto the glass substrate. Fig. 3b depicts the corresponding elastic modulus and hardness evolution with the penetration depth. Fig. 3 highlights the general characteristics of the nanoindentation tests conducted in this study, in which the elastic modulus remained constant with increasing penetration depth, and the hardness reached an asymptotic value at a depth significantly lower than the maximum penetration. The analysis of the data obtained from 80 indentation tests on the glass substrate, using the Oliver and Pharr methodology [29,30], yielded an average elastic modulus of 73 GPa and a hardness of 6.3 GPa [34], with standard deviations of 1 GPa and 0.1 GPa, respectively. These average values were obtained from a total of 80 indentations carried out using CSM, as it is explained in the methods section. These values fall within the typical range reported for this material, highlighting the good reliability of the calibration as well as the appropriateness of the testing methodology and data processing. Furthermore, the standard deviations are below 10% of the mean values, demonstrating the robustness of the recorded data. Based on these results, nanoindentation tests on the multilayer system constituting the solar cells can be confidently undertaken.

Subsequently, indentation tests were carried out on the solar cell coatings. The indentation procedure was similar for the samples of both types of solar cells. A diamond Berkovich indenter was used, applying the calibration performed on silica and selecting the CSM module. Indentations were performed with an oscillation frequency of 35 Hz and an amplitude of 2 nm, reaching a maximum penetration depth of 2500 nm, following the same methodology used for the indentations on the glass substrate. This depth ensured that the indenter could penetrate

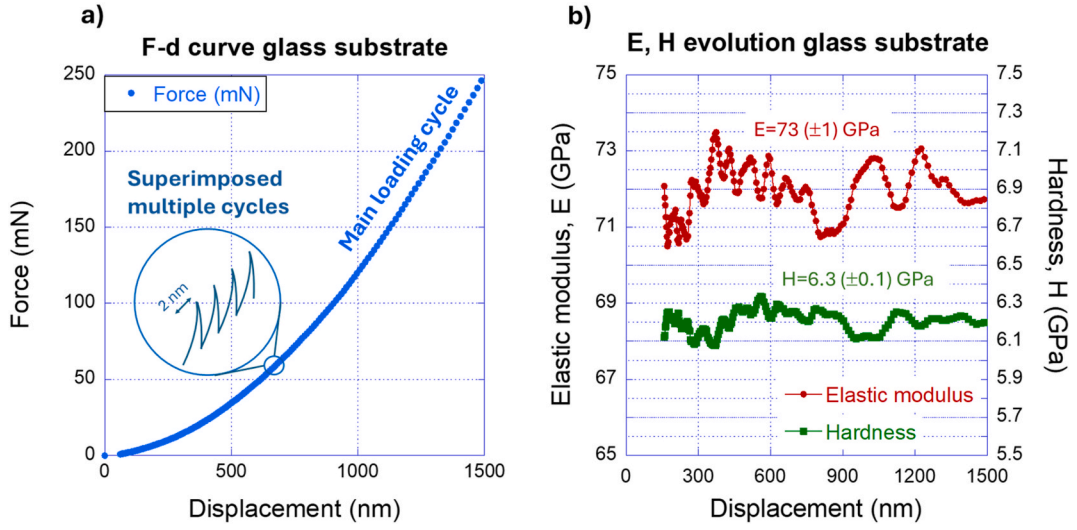


Fig. 3. Representative results of nanoindentation test on glass substrate: a) force-displacement curve; b) elastic modulus and hardness evolution. The E and H mean values, showed in the figure, were obtained for a total of 80 indentations carried out using CSM.

through all layers and reach the glass substrate with sufficient margin. For each type of coating, arrays of 150 indentations were programmed, spaced 100 μm apart. It should be noted that the nanoindentation experiments were performed on samples that did not include the Spiro-OMeTAD hole-transport layer or the Au top electrode. Therefore, the mechanical characterization reported in this work corresponds exclusively to the Glass/FTO/c-TiO_2/m-TiO_2/perovskite structure described in Table 1.

Fig. 4 shows a representative image of three residual indentation imprints selected from the array of 150 indentations performed on the solar cell. A key feature of this image is the high reproducibility of the residual indentation geometry, which provides confidence in the reproducibility of the load, F, and contact stiffness, S, measurements obtained during the indentation process through the Continuous Stiffness Measurement (CSM) methodology.

In addition, a representative load-displacement (F-d) curve and contact stiffness-displacement (S-d) curve are included in the same figure. The quantities directly measured during the nanoindentation test are highlighted. For each displacement value, d_i, the corresponding indentation load, F_i, and contact stiffness, S_i, were determined. These data constitute the primary experimental output of the nanoindentation test and were subsequently used to calculate the elastic modulus and hardness according to the Oliver and Pharr methodology. Consequently, each individual indentation provides a complete set of load, displacement, and contact stiffness data over the entire penetration depth range, allowing the elastic modulus and hardness to be continuously determined as a function of penetration depth. For each indentation, 1050 values of elastic modulus and hardness were obtained as a function of penetration depth, approximately one data point every 1.2 nm.

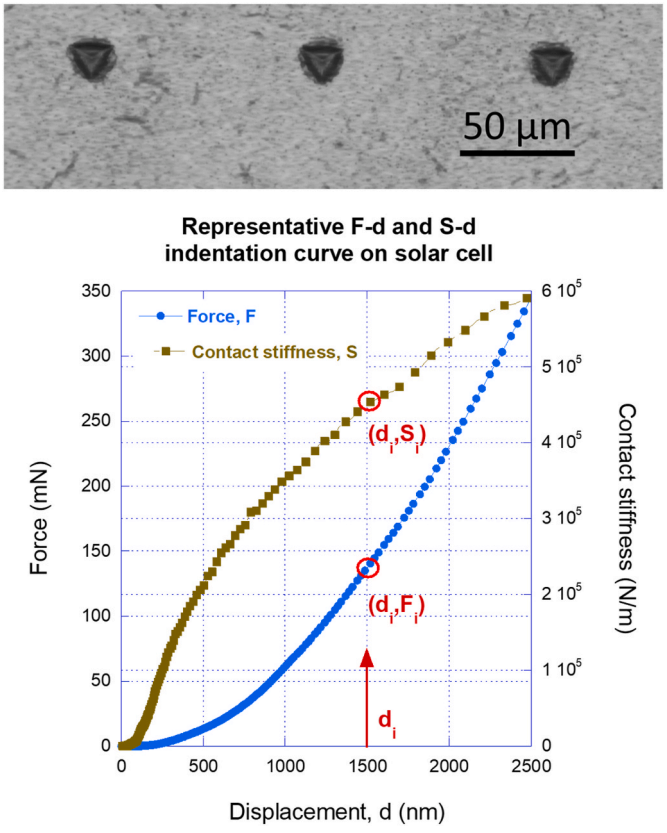


Fig. 4. Representative residual indentation imprints extracted from the matrix of 150 nanoindentation tests performed on the solar-cell surface. Additionally, representative load-displacement (F-d) and contact stiffness-displacement (S-d) curves obtained using the Continuous Stiffness Measurement (CSM) technique are also included.

Therefore, the set of mechanical property values obtained from the nanoindentation tests was sufficient to analyse the properties of each coating and perform a statistical analysis.

The statistical study can be carried out following different strategies depending on the type of information required and the depth at which the analysis is to be performed. A first approach consists of reducing the statistical treatment to the calculation of a mean value and its corresponding standard deviation, obtained from the elastic modulus and hardness data recorded during indentation within the thickness range corresponding to each layer of the solar cell (thickness data statistical analysis, TSA). This procedure can be carried out because the thicknesses of each of the layers constituting the solar cell coating system are precisely known. In other words, this statistical analysis procedure requires prior knowledge of the thickness of each layer. This, in turn, necessitates exhaustive control of the manufacturing process. For a more rigorous analysis, deconvolution procedures may be applied to estimate the probability distributions associated with each layer (deconvolution statistical analysis, DSA). The advantage of this method is that prior knowledge of the coating thicknesses is not required, since it is not necessary to segment the data according to the depth ranges corresponding to each individual layer. With this approach, the property values of the different layers are naturally generated and discriminated. In this work, both methodologies have been implemented, allowing us to assess their reliability in determining the mechanical properties of the individual layers that constitute the device.

3. Results and discussion

3.1. Thickness-discriminated statistical analysis

Depth-dependent nanoindentation enabled direct access to the mechanical response of the multilayer solar cell architecture across the full coating thickness. The use of continuous stiffness measurement (CSM) allowed the evolution of elastic modulus and hardness to be tracked as a function of penetration depth, revealing distinct mechanical signatures associated with individual functional layers through an initial statistical treatment of the mechanical data. To establish a first layer-resolved comparison, elastic modulus and hardness values were analysed over depth ranges corresponding to the thickness of each layer, providing representative mean values and variability trends that form the basis for the subsequent mechanical analysis.

The elastic modulus values of the individual layers in the solar cell structure vary significantly depending on the material and its microstructure. The elastic modulus of methylammonium lead iodide ($MAPbI_3$) perovskite films has been reported to vary depending on the fabrication method, crystallinity, and presence of additives. For instance, studies using nanoindentation and atomic force microscopy have reported values around 14–17 GPa for pristine $MAPbI_3$ films [35,36]. Additionally, other studies on the mechanical properties of $MAPbI_3$ also measured the E value with nano-indentation giving a range of values between 10 GPa and 20 GPa depending on dwell time and lattice plane [37–40]. Feng et al. investigated the elastic properties and anisotropy of $MABX_3$ (B=Pb, Sn; X = Br, I) using first-principles calculations based on density functional theory (DFT). They reported a E value of 22.2 GPa for $MAPbI_3$ [41]. Other studies have reported even broader ranges of elastic modulus values (from 10 to 28 GPa) [15,16,42]. Faghihnasiri et al. [43] also reported E values for $MAPbI_3$ that ranged from 15 GPa to 34.5 GPa. However, Liu et al. [44] explored the role of 2D structure pentanamine iodide in improving the properties of 3D $MAPbI_3$ perovskite thin films from the perspective of Young's modulus matching. They reported a value of 47.1 GPa for $MAPbI_3$ pristine perovskite films and 35.1 GPa for the perovskite film treated with 3.3% pentanamine iodide. These wide variations in the E values using the nanoindentation method are attributed to its sensitivity to the following: synthesis method, quality, and orientation of the single-crystals. Also, although nanoindentation may be performed on

(100) surfaces of bulk single-crystals, that does not imply that the measured E is in <100> direction due to the complex three-dimensional (3D) geometry inherent to the indentation process. Based on all the information gathered from previous studies, it can be summarized that the elastic modulus for different perovskite formulations lies in the range of 10 to 28 GPa. Therefore, it is expected that the perovskites corresponding to the type-1 and type-2 cells analysed in this work will exhibit elastic modulus values within this range. Since the elastic modulus is an intrinsic property, the reported range of values may be used to assess the reliability of the results obtained from the statistical analysis of the nanoindentation-derived data.

For the mesoporous TiO_2 layer, the elastic modulus typically ranges between 10 and 50 GPa, influenced by the degree of porosity and synthesis method [45–47]. In contrast, the compact TiO_2 layer exhibits higher stiffness, with reported values of 65 GPa for films deposited via reactive evaporation and up to 147 GPa for those produced by ion plating, according to Anderson and Ottermann [47,48]. For the Fluorine-doped Tin Oxide (FTO) layer, the elastic modulus has been reported in the range of 100 to 130 GPa, depending on the doping level and deposition conditions, as described by Haddad et al. [49] and Tuyen et al. [50].

The hardness of methylammonium lead iodide ($MAPbI_3$) perovskite films has been investigated in various studies, typically using nanoindentation techniques. Similar tendency can be inferred from hardness comparison. The hardness of thin film materials used in solar cell architectures varies significantly depending on their microstructure and deposition method. Consequently, hardness values for perovskites also fall within a certain range. Sun et al. [40] reported values of 0.42–0.46 GPa for $CH_3NH_3PbI_3$, 0.26–0.31 GPa for $CH_3NH_3PbBr_3$, and 0.25–0.29 GPa for $CH_3NH_3PbCl_3$. Reyes-Martínez et al. [51] obtained hardness values of 0.35 GPa for $CH_3NH_3PbBr_3$ and 0.55 GPa for $CH_3NH_3PbI_3$. Ramírez et al. [38] reported values ranging from 0.42 to 1 GPa. Additionally, Chen et al. [52] measured hardness values ranged between 0.38 and 0.69 GPa. Furthermore, Spina et al. [39] investigated the mechanical characteristics of $MAPbI_3$. They observed an influence of the exposure time to humidity on the hardness values of the perovskite, reporting a value of 1 GPa at 0 days and a gradual decrease to 0.3 GPa after 100 days. Overall, the hardness values reported for different perovskites can be summarized as lying within the interval of 0.4–1 GPa. For mesoporous TiO_2 films, the hardness is strongly influenced by porosity and crystalline phase, typically ranging from 0.5 to 2 GPa, with lower values corresponding to higher porosity. This trend is discussed in detail by Lionello et al. [53]. In contrast, compact TiO_2 films exhibit significantly higher hardness values, typically around 5 to 8 GPa, depending on the deposition technique and phase composition [54,55]. For fluorine-doped tin oxide (FTO) films, Vickers hardness measurements indicate values in the range of 4 to 6 GPa, depending on doping concentration and film thickness [55,56]. However, the scientific literature reveals that the hardness of Fluorine-Doped Tin Oxide (FTO) thin films can be higher depending on the Fluorine/Tin ratio. Tuyen et al. [50] reported hardness values of 5.6 ± 0.2, 6.9 ± 0.3, 12.3 ± 0.4, and 10.2 ± 0.3 GPa for FTO films deposited at 0, 0.1, 0.5, and 1.0 F/Sn ratios, respectively. Comparable ranges of values could be observed on the type 2 solar cells, except for the CsRbFAMAPb$(IBr)_3$ perovskite layer, whose elastic modulus and hardness values have not been reported in any previous studies, and therefore no reference values are available.

Table 2 summarizes the ranges of elastic modulus and hardness values reported in the literature for the different layers of type-1 solar cells.

Fig. 5a shows the values of elastic modulus and hardness obtained for solar cell type 1, from the data recorded during indentation within the thickness range corresponding to each layer of the solar cell, TSA analysis. This figure presents the elastic modulus values, yielding 65 GPa for the perovskite layer, 98 GPa for the mesoporous TiO_2 layer, 101 GPa for the compact TiO_2 layer, 102 GPa for the FTO layer, and 73 GPa for the glass substrate. The latter value corresponds to the nominal elastic modulus of glass (Fig. 3b). However, significant discrepancies were observed in the values obtained for the other layers, mainly perovskite and m-TiO_2, when compared to those reported in previous studies.

Table 2
Reference values of elastic modulus and hardness corresponding to the solar cell layers (type-1).

Material/layer	E (GPa) values from references	H (GPa) values from references
$MAPbI_3$ perovskite	10-28	0.4-1.5
TiO_2 mesoporous layer	10-50	0.5-2
TiO_2 compact layer	65-147	5-8
FTO	100-130	5.5-12
Glass substrate	72	6.3

Significant differences were also observed in the hardness values. Specifically, an average value of 3.08 GPa was obtained for the depth range corresponding to the perovskite layer, a value that lies significantly outside the nominal range (Table 1). Significant deviations from the nominal values were also found for the remaining layers. Differences of 65%, 30%, and 24% with respect to the closest values within their nominal ranges (Table 1) were reported for the mesoporous TiO_2, compact TiO_2, and FTO layers, respectively. It should be noted that this error is negligible in the value obtained for the glass substrate. This latter result serves as evidence that the testing methodology is valid and that another phenomenon is responsible for the discrepancies observed relative to the expected values.

Fig. 5b, c and 5d shows the mean values and the corresponding standard deviations of the elastic modulus and hardness obtained from the three samples of the Type-2 solar cell. In this case, no comparison can be made for the values of both mechanical properties measured in the perovskite layer of this type of solar cell, since no reference data are available; however, a comparison can be performed for the remaining layers. When comparing the values obtained from the nanoindentation methodology, using a statistical treatment based solely on calculating the mean values and standard deviations of the results corresponding to each depth range included within the thickness of each layer, significant discrepancies with respect to the nominal values were again observed. Thus, value ranges of 90–105 GPa and 3–3.5 GPa were obtained for the elastic modulus and hardness, respectively, in the mesoporous TiO_2 layer. These ranges are significantly higher than the nominal values reported for this material (Table 2). A similar situation was observed for the compact TiO_2 layer, for which the calculated ranges were 90–109 GPa for the elastic modulus and 3–3.7 GPa for the hardness. Once again, these ranges differ markedly from the nominal value ranges (Table 2). In the case of the FTO layer, the differences with respect to the expected values were smaller. An elastic modulus value of 110 GPa was reported, which lies within the nominal range, and a hardness value of 4.3 GPa, which is close to the lower bound of the expected range for this material. Nevertheless, most of the values of both properties obtained through this statistical data analysis methodology exhibit significant discrepancies when compared with their nominal counterparts (Table 1). As in the Type-1 solar cell, the values of both properties obtained for the glass substrate were very close to the expected values (Table 1). Therefore, in this type of solar cell, the existence of a phenomenon acting as a source of discrepancy with respect to the nominal values is also confirmed, and this phenomenon is not related to the nanoindentation methodology, such as calibration, cycle frequency, or data acquisition resolution.

Consequently, these discrepancies may be due to the influence of the surrounding layers on the measurements recorded within each individual layer. The property values selected to calculate the mean and standard deviation are likely determined primarily by the response of the layer located at the depth where the measurements are being taken. However, there is also an influence from the underlying layers, due to the volume affected by the deformation fields induced by the

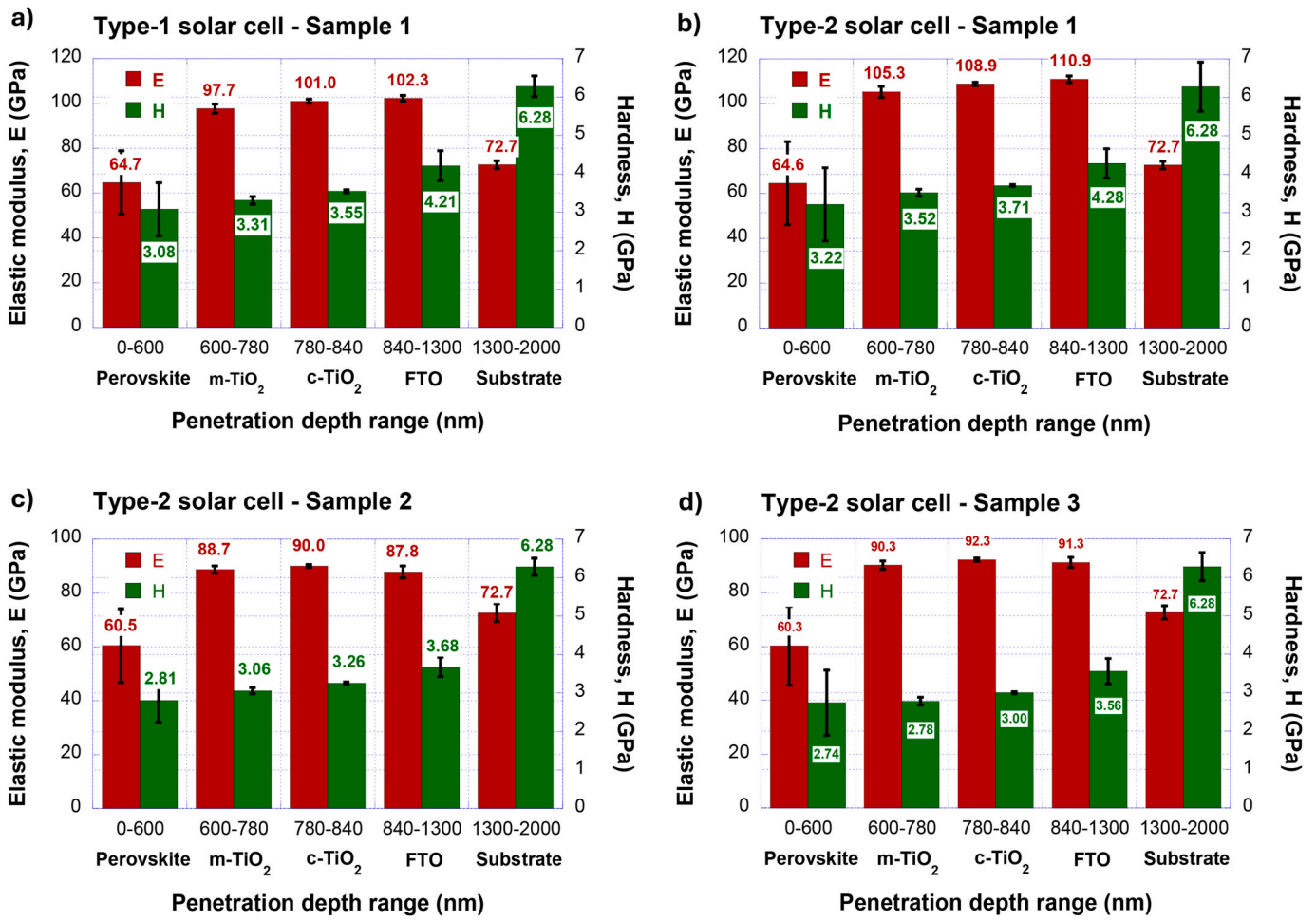


Fig. 5. Values of elastic modulus, E and hardness, H for different layers of the solar cell: a) type 1; b), c) and d) type 2.

indentation process. Previous studies have reported that, when nanoindentation is performed on a coating–substrate system, the measured elastic modulus and hardness are governed by the interaction of the deformation fields developed in both the coating and the underlying substrate. As the penetration depth increases, the stress and strain fields beneath the indenter extend progressively further into the material, eventually reaching the coating–substrate interface and activating deformation in the substrate. Once this occurs, the measured response no longer represents the intrinsic mechanical properties of the coating, but rather a composite response of the coupled coating–substrate system. This effect becomes particularly significant when the maximum indentation depth exceeds approximately 10% of the coating thickness, a phenomenological criterion originally proposed to minimize substrate influence. Finite element simulations and experimental studies have shown that, even at shallow depths, the elastic field can extend several times the contact radius, making the elastic modulus especially sensitive to substrate stiffness, while hardness may remain coating-dominated over a slightly wider depth range. The magnitude and direction of the deviation depend on the elastic and plastic mismatch between coating and substrate, leading to overestimation or underestimation of the coating properties depending on whether the substrate is stiffer or more compliant than the coating [56]. It may explain the discrepancies observed between nominal layers' properties (Table 1) and nanoindentation derived values (Fig. 5).

These discrepancies may be attributed to the effect of adjacent layers in nanoindentation tests. This suggests that a different approach may be necessary, one oriented toward a more statistical analysis.

3.2. *Statistical separation of layer-specific mechanical responses*

An alternative statistical analysis procedure was selected to discriminate the representative values of both mechanical properties corresponding to each layer of both solar cell types operating over the nanoindentation data.

To achieve this objective, a conditional statistical deconvolution procedure was implemented, combining hybrid histogram deconvolution with a Gaussian Mixture Model (GMM) [57]. The method starts from the global histogram obtained from the nanoindentation data and assumes that this distribution results from the superposition of multiple statistically independent mechanical responses associated with different layers of the system. Accordingly, the overall histogram is decomposed into a set of partial histograms, each represented by a Gaussian distribution characterized by a single, well-defined peak, a mean value, and an associated standard deviation. The parameters of the Gaussian components are determined through an optimization process aimed at minimizing the reconstruction error between the experimental global histogram and the weighted sum of the partial distributions. A key constraint is imposed during the deconvolution: at least one Gaussian component is forced to exhibit a peak centered at the known mechanical property value (elastic modulus and hardness) of the substrate (glass). This constraint anchors the solution physically and reduces ambiguity in the allocation of the remaining components. Through this conditional deconvolution strategy, the contributions of different layers within the coating stack can be statistically separated, allowing the identification of distinct mechanical populations within the dataset. The number of partial Gaussian distributions generated by the deconvolution process

depends on the complete raw data histogram. Consequently, the Gaussian mixture model was used to identify statistically distinct mechanical populations within the dataset without imposing any predefined correspondence between populations and individual layers, except for the substrate constraint used for calibration purposes. The statistical indentation approach and subsequent deconvolution procedures have already been extensively reported and validated in heterogeneous multiphase systems. Therefore, agreement between the extracted properties and independent literature data is used here as a consistency check supporting the physical interpretation of the identified populations. The populations corresponding to glass, FTO, compact TiO_2 and mesoporous TiO_2 were subsequently identified through comparison with literature-reported ranges of elastic modulus and hardness. The remaining population, which could not be consistently assigned to any of the previously identified layers, was therefore attributed to the perovskite absorber, in agreement with the known architecture of the solar-cell stack. Importantly, no elastic modulus or hardness constraints associated with the perovskite layer were introduced during the deconvolution procedure. Thus, the identification of the perovskite population was performed a posteriori, only after the assignment of all layers for which independent reference data were available.

To carry out this process, a Python script has been developed that reads the data and generates the partial histograms while satisfying the imposed boundary conditions. In particular, Gaussian Mixture Model (GMM) was applied using the Scikit-Learn package. Subsequently, the histograms obtained after applying this methodology to the elastic modulus and hardness values of both types of solar cells are presented. The average, μ, and standard deviation, σ, values of the corresponding partial histograms were included. Additionally, the RMSE and w parameters were also included. In the Gaussian deconvolution process, the RMSE is used as a quantitative metric to evaluate the quality of the fit between the experimental data histogram and the distribution reconstructed from the linear combination of Gaussian components. Specifically, RMSE measures the average deviation between the experimental histogram and the model prediction, with lower RMSE values indicating a more accurate reconstruction of the underlying data distribution. In relative terms, RMSE values that are small compared to the overall amplitude or variance of the histogram can be interpreted as indicative of a good fit, whereas comparatively large RMSE values reflect a poor agreement between the reconstructed distribution and the experimental data, suggesting an insufficient number of Gaussian components or inadequately estimated parameters. The parameter w, on the other hand, represents the statistical weight of each Gaussian component within the mixture model and quantifies its relative contribution to the overall distribution. In practical terms, w reflects the fraction of data points associated with a given mechanical response, such that Gaussian components with higher weights correspond to more dominant contributions to the measured response, while lower weights indicate minor or less prevalent contributions. It should be noted that the weighting factor w associated with each Gaussian component represents its relative contribution to the overall distribution of measured mechanical properties rather than the physical thickness fraction of the corresponding layer. Since the deconvolution is performed on the complete CSM dataset, each indentation contributes a large number of elastic modulus and hardness measurements over the entire penetration range. Furthermore, the mechanical response recorded at a given depth is affected by the indentation interaction volume and by the overlap between neighbouring layers. Consequently, the Gaussian weights are not expected to scale directly with the nominal thickness of the constituent layers within the solar-cell stack.

Because the multilayer architecture consists of five physically distinct layers, the deconvolution output was subsequently subjected to a condensation procedure aimed at obtaining physically meaningful mechanical populations. This condensation stage is not part of the fitting procedure itself but rather a physically guided post-processing step. The purpose of the condensation procedure was to merge neighbouring Gaussian components that originate from the statistical decomposition of the same mechanical population. Due to experimental scatter, layer interactions, substrate influence, and the intrinsic tendency of Gaussian Mixture Models to partition broad distributions into several adjacent components, the deconvolution process may generate a number of mathematical components larger than the number of physically distinct layers. Consequently, multiple Gaussian components may represent different portions of the response of a single layer rather than independent material layers. The condensation procedure reduces this overparameterisation by grouping statistically similar neighbouring components while preserving the quality of the histogram reconstruction. The condensation criterion was applied systematically to all datasets and was independent of the expected elastic modulus or hardness values of the individual layers. This criterion was based on grouping those Gaussian components whose mean values, μ, fall within a predefined interval $\mu \pm 0.1\sigma$, where σ is the standard deviation of the condensed distributions. The value of 0.1σ provided the best compromise between preserving physically meaningful populations and avoiding overparameterization.

Fig. 6 shows the histograms for elastic modulus and hardness of the type 1 solar cell. As can be observed in this figure, the complete histogram of the raw data for both elastic modulus (Fig. 6a) and hardness (Fig. 6b) is characterized by the absence of a clear number of significant peaks that could be directly associated with the most probable values of the different coating layers. This prevents the direct inference of elastic modulus and hardness values from the analysis of the full histogram alone, thereby justifying the application of the deconvolution procedure described above.

In Fig. 6, the partial histograms generated through the deconvolution process are drawn superimposed onto the complete histogram. For both elastic modulus and hardness, the number of Gaussian partial histograms obtained exceeded the number of layers in the coating. Consequently, for the Type-1 solar cell, it was necessary to apply the condensation procedure following the criterion which will be described in the section Methods, Conditional deconvolution statical procedure. As a result of this condensation process, five partial histograms were generated, matching the number of coating layers, for both elastic modulus and hardness. The mean values and standard deviations corresponding to each of these five partial histograms are summarized in Table 3.

In the case of the elastic modulus (Fig. 6a), a total of nine partial Gaussian distributions were generated through the deconvolution process. The resulting root mean square error (RMSE) was 0.014, which indicates a good quality of fit. It is worth noting that one of the partial distributions exhibits a mean value of 71.7 GPa with a standard deviation of 3.51 GPa, values that are very close to those corresponding to the glass substrate. This result provides confidence in the reliability and physical consistency of the established deconvolution procedure. Regarding the values obtained after applying the condensation process to reduce the number of Gaussian components to five (Table 3), it can be observed that the resulting RMSE remains low, thereby preserving the good quality of the fit. Moreover, a distribution with elastic modulus values similar to those of the glass substrate is still obtained, further supporting the robustness of the deconvolution and condensation methodology.

By comparing the mean values of the partial elastic modulus distributions with the nominal ranges presented in Tables 2 and it is possible to establish an association between each partial distribution and the corresponding material of the solar coating. To this end, each mean value of the partial distributions is selected and matched to the nominal value range in Table 2 within which it may fall. The last column of Table 3 identifies the materials of the Type-1 solar coating whose nominal elastic modulus ranges include the mean value of each partial distribution (Fig. 6a).

For hardness (Fig. 6b), the number of partial distributions generated was thirteen, which is noticeably higher than in the case of the elastic

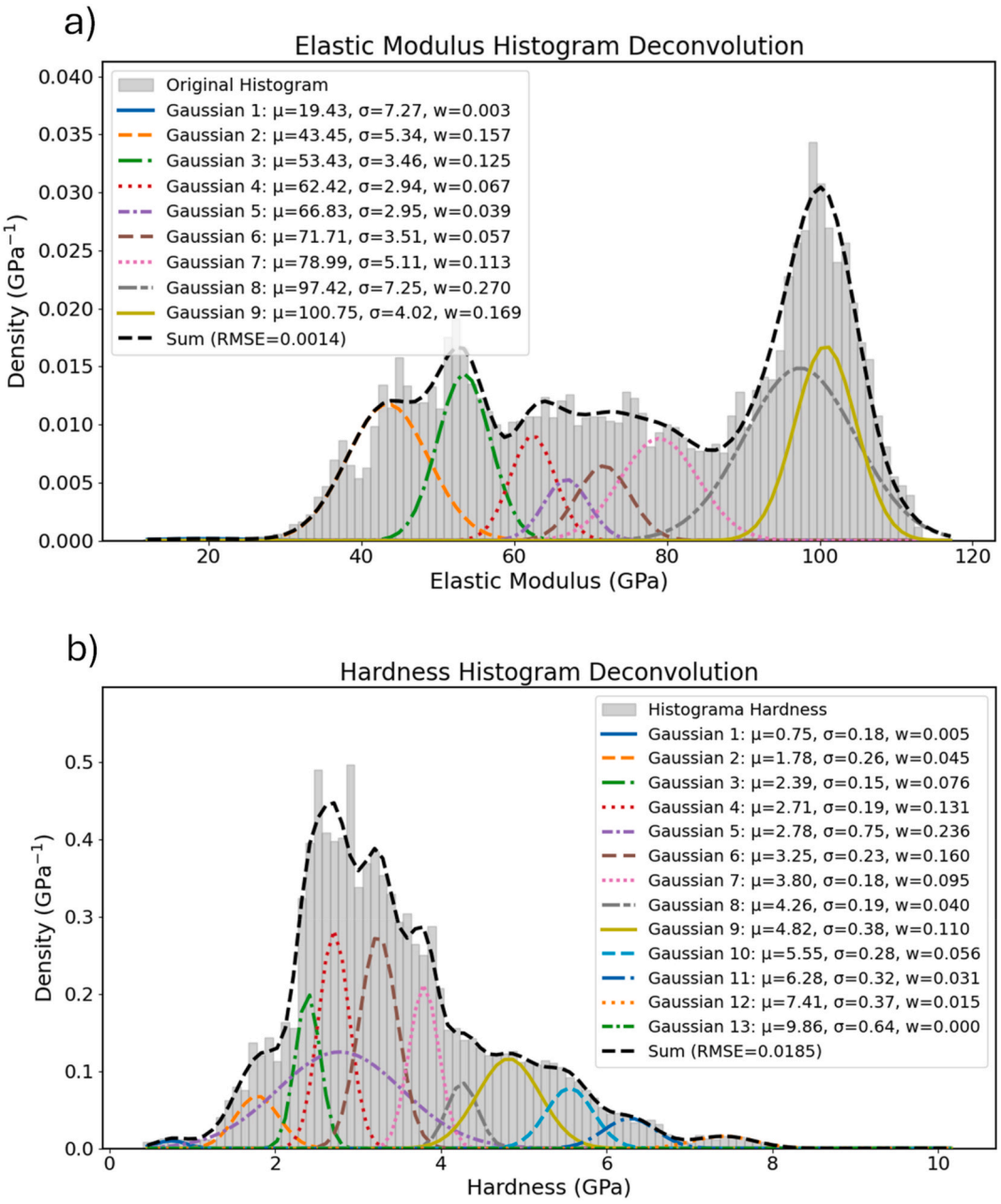


Fig. 6. Histograms for elastic modulus (a) and hardness (b) of the type 1 solar cell. Partial gaussians distributions are drawn superimposed to the histogram of the raw data. Values of the mean, standard deviation and weight (*w)* parameter for each partial distribution are included. Additionally, RMSE value is also showed.

modulus. Nevertheless, an RMSE value of 0.019 was obtained, which is sufficiently small to consider the fit to be of good quality. In addition, one of the partial distributions exhibits a hardness value similar to that measured for the glass substrate (Table 2), providing confidence in the hardness values derived from this statistical analysis.

As performed for the elastic modulus, it was also necessary to apply a condensation procedure to the set of Gaussian distributions, resulting in a total of five distributions. The mean values, standard deviations, and weights of each of these condensed distributions are summarized in Table 4, together with the corresponding RMSE value for the five-component fit. The outcome of this condensation procedure once again yields a distribution with a mean hardness value of 6.28 GPa, which is consistent with that of the glass substrate.

A similar procedure for associating partial Gaussian distributions with the corresponding layer materials, as carried out for the elastic modulus, was also applied to hardness. The materials associated with each of the five Gaussian distributions are reported in the last column of Table 4. As in the case of the elastic modulus, the mean hardness values obtained could be successfully identified with the layers corresponding to the materials used in each layer of the Type-1 solar coating. Nevertheless, it could be observed that in some cases interference between the deformation fields of adjacent layers occurs, leading to hardness values that represent a combination of their corresponding nominal values. This is the case for Gaussian distribution 3, whose mean value is likely associated with the combined effect of the mesoporous and compact TiO_2 layers.

The five layers of the Type-1 solar coating were thus identified together with their corresponding mechanical properties. Accordingly, an elastic modulus of 19 GPa and a hardness of 0.75 GPa were reported for the $MAPbI_3$ perovskite layer. These values fall within the nominal ranges for both properties, according to the identification criterion explained above. Consequently, these values are similar to those

Table 3
Elastic moduli mean values, standard deviations and weights corresponding to each of the five condensed partial histograms. RMSE value is also included. The last column shows the material layer obtained from the comparison with Table 2.

Gaussian distributions	Mean, μ (GPa)	Standard deviation, σ (GPa)	Weight, *w*	RMSE	Material layer
Gaussian 1: C1	19.43	7.27	0.003	0.002	$MAPbI_3$ pervskite
Gaussian 2: C2	47.86	6.76	0.282		TiO_2 mesoporous
Gaussian 3: C3	71.75	7.91	0.275		Glass substrate
Gaussian 4: C4	97.42	7.25	0.270		TiO_2 compact
Gaussian 5: C5	100.75	4.02	0.169		FTO

Table 4
Hardness means values, standard deviations and weights corresponding to each of the five condensed partial histograms. RMSE value is included. The last column shows the material layer obtained from the comparison with Table 2.

Gaussian distributions	Mean, μ (GPa)	Standard deviation, σ (GPa)	Weight, *w*	RMSE	Material layer
Gaussian 1: C1	0.747	0.183	0.005	0.061	$MAPbI_3$ pervskite
Gaussian 2: C2	1.783	0.261	0.045		TiO_2 mesoporous
Gaussian 3: C3	3.507	1.123	0.936		TiO_2 mesoporous + TiO_2 compact
Gaussian 4: C4	6.280	0.372	0.015		Glass substrate
Gaussian 5: C5	9.862	0.642	0.001		FTO

reported in the literature for this type of perovskite. This confirms the reliability of the proposed methodology for identifying mechanical properties based on statistical indentation and subsequent deconvolution analysis.

Therefore, a similar procedure was applied to the elastic modulus and hardness values obtained from the nanoindentation tests onto the three samples of the type 2 solar cell in order to determine the values of both properties for the $CsRbFAMAPb(IBr)_3$ perovskite layer.

Fig. 7 shows the partial gaussian distributions of elastic modulus and hardness for the three samples of type 2 solar cell. It was observed that the deconvolution process yielded a set of five partial histograms whose combination reconstructed the complete histogram for the three samples, for both elastic modulus and hardness. The only case in which a larger number of histograms was obtained corresponded to Sample 3 for the hardness values (Fig. 7f). In this case, the histogram grouping procedure described previously was applied, resulting in five partial histograms. Fig. 7f includes a table summarizing the mean values and standard deviations of these distributions. For all samples, the deconvolution method consistently generated one distribution whose mean elastic modulus and hardness values were similar to the nominal values of the glass substrate. For the remaining distributions, a comparison was performed with the nominal value ranges of both properties summarized in Table 2.

Table 5 presents the mean values of the distributions obtained from the three samples of the Type-2 solar cell, together with the associated materials resulting from the comparison with the nominal values. This comparison was necessarily carried out only for the layers that are common to both solar cell types, namely the mesoporous and compact TiO_2 layers and the FTO layer. The remaining unassigned distribution corresponds to the one providing the elastic modulus and hardness values of the $CsRbFAMAPb(IBr)_3$ perovskite layer, reporting an average value of 19.5 GPa and 2.7 GPa for the elastic modulus and hardness, respectively.

Therefore, based on the statistical analysis of the results, it can be concluded that the $CsRbFAMAPb(IBr)_3$ perovskite in the type-2 solar cell exhibits an elastic modulus similar to that of the perovskite in the type-1 cell, and hardness values significantly higher than those measured in the reference $MAPbI_3$ device and higher than the ranges commonly reported for $MAPbI_3$ in the literature.

Tables 4 and 5 provide the average values for elastic modulus and hardness for both perovskites. From these values, the corresponding H/E and H^2/E ratios were estimated. The magnitude H/E can be considered as a measure of the material's ability to bear elastic deformation. In other words, this ratio is related to the deformation limit before permanent damage is caused. On the other hand, H^2/E can be understood as a measure of the material's ability to store elastic energy. Both magnitudes are significant in the mechanical performance of the material. The values for both ratios were 0.038 and 0.029, respectively, for $MAPbI_3$ and 0.138 and 0.373, respectively, for $CsRbFAMAPb(IBr)_3$ perovskite. The lower H/E ratio obtained for $MAPbI_3$ is a warning of its greater sensitivity to brittle failure. On the other hand, the higher value of the H^2/E ratio of $CsRbFAMAPb(IBr)_3$ reveals a greater resistance to permanent deformation. Consequently, it is expected that the $CsRbFAMAPb(IBr)_3$ perovskite will exhibit greater mechanical performance during its operation in service.

4. Conclusions

The layer-resolved mechanical analysis presented in this work provides new insight into the mechanical behaviour of complete perovskite solar cell architectures. By combining depth-dependent nanoindentation with a conditional statistical deconvolution approach, elastic modulus and hardness could be consistently resolved across individual functional layers within working device stacks.

The close agreement between the extracted mechanical properties of the glass substrate, charge-transport layers and $MAPbI_3$ absorber and previously reported values demonstrates the robustness and reproducibility of the proposed methodology. Importantly, this consistency across two different device architectures confirms that the observed mechanical trends are intrinsic to the materials rather than artefacts of the analysis.

Beyond methodological validation, the results reveal a marked mechanical distinction between single-cation and multi-cation perovskite absorbers. While the elastic modulus of $CsRbFAMAPb(IBr)_3$ remains comparable to that of $MAPbI_3$, its substantially higher hardness indicates a significantly enhanced resistance to localized plastic deformation. This decoupling between stiffness and hardness highlights the potential of compositional engineering to improve mechanical resilience without compromising structural compliance.

From a mechanical perspective, the increased hardness of the multication perovskite indicates a greater resistance to induced deformation. Although this behaviour may be relevant to other aspects of mechanical performance, including fracture resistance and interfacial stability, these relationships remain to be established and require further investigation in future studies. These findings underscore the importance of system-level mechanical characterization and suggest that compositional optimization can significantly modify the mechanical response of perovskite absorbers.

Furthermore, the mechanical properties reported in the present work can be regarded as reference values for the studied device architectures. The availability of layer-resolved baseline values for elastic modulus and hardness provides a quantitative starting point against which future measurements on aged or environmentally exposed devices may be compared. In this sense, the methodology proposed here may not only be used to characterize multilayer perovskite solar cells, but also to quantify the evolution and eventual degradation of the mechanical

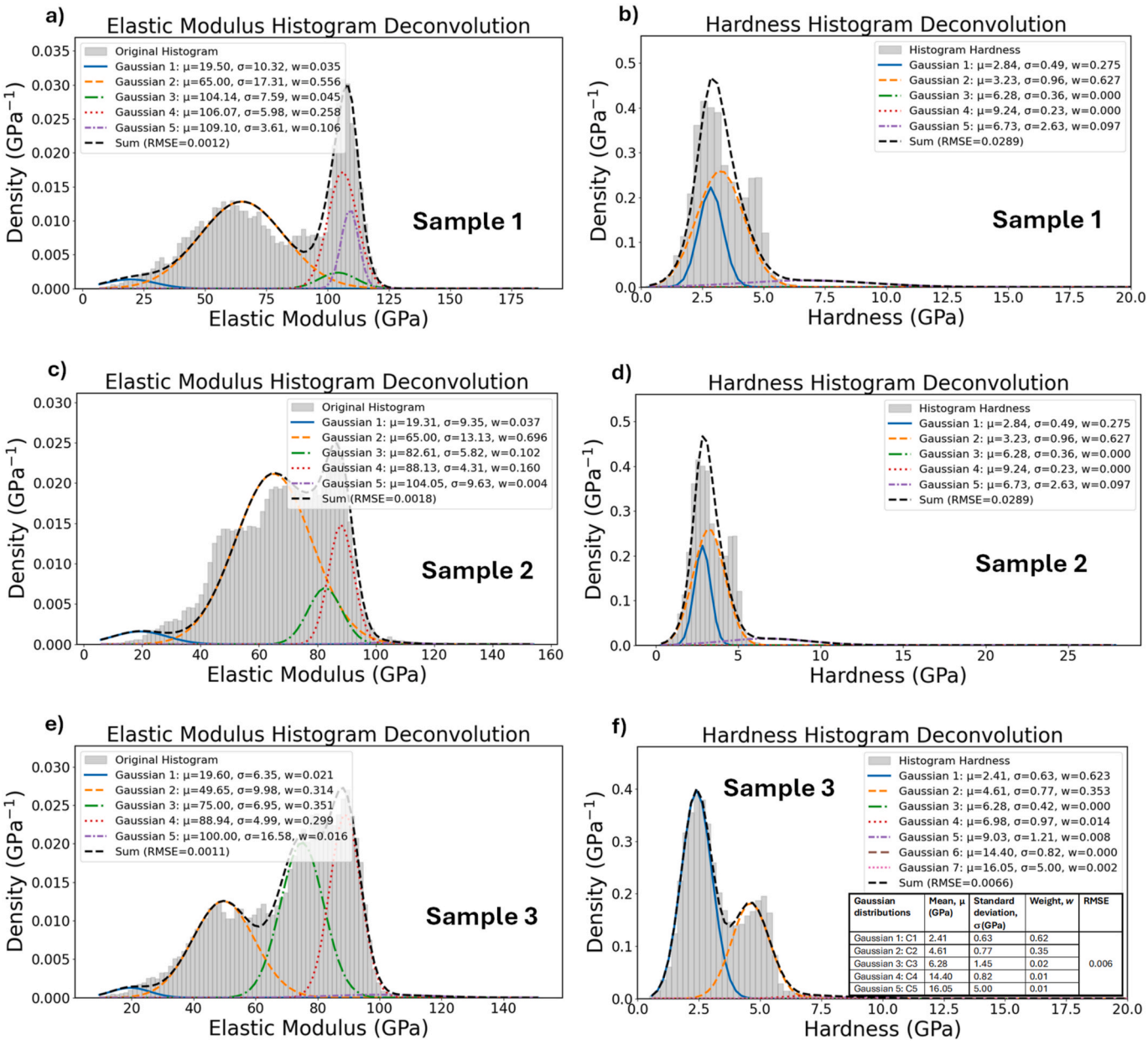


Fig. 7. Histograms for elastic modulus (a) and hardness (b) of the type 2 solar cell. Partial gaussians distributions are drawn superimposed to the histogram of the raw data. Values of the mean, standard deviation and *w* parameter for each partial distribution are included. Additionally, RMSE value is also showed. a), c), e) elastic modulus distributions for the three samples; b), d), f) hardness distributions for the three samples.

Table 5
Elastic moduli and hardness mean values and the corresponding standard deviations extracted from the statistical analysis carried out onto the data from the three samples of type 2 solar cell. The last column shows the material layer obtained from the comparison with Table 2.

E Mean, μ (GPa)	E Standard deviation, σ (GPa)	H Mean, μ (GPa)	H Standard deviation, σ (GPa)	Material layer
19.47	8.67	2.694	0.537	CsRbFAMAPb $(IBr)_3$ perovskite
49.65	9.97	3.690	0.897	TiO_2 mesoporous
94.38	5.09	9.287	2.025	TiO_2 compact
104.38	9.94	11.507	1.818	FTO
68.33	12.46	6.280	0.722	Glass substrate

properties of individual layers during service conditions.

CRediT authorship contribution statement

Miguel Ángel Garrido-Maneiro: Writing – original draft, Methodology, Investigation, Formal analysis, Data curation, Conceptualization. **María del Carmen López-González:** Resources, Investigation, Data curation, Conceptualization. **Belén Arredondo:** Writing – review & editing, Validation, Funding acquisition, Formal analysis, Conceptualization. **Beatriz Romero:** Writing – review & editing, Writing – original draft, Validation, Supervision, Funding acquisition, Formal analysis, Conceptualization. **Pedro Poza:** Writing – review & editing, Writing – original draft, Validation, Supervision, Funding acquisition, Conceptualization. **Jesús Rodríguez:** Writing – review & editing, Writing – original draft, Validation, Supervision, Project administration, Funding acquisition, Conceptualization.

Declaration of competing interest

The authors declare that they have no known competing financial interests or personal relationships that could have appeared to influence the work reported in this paper.

Acknowledgements

The authors wish to thank Universidad Rey Juan Carlos for the financial support under Project GI022. The authors wish to thank to the Spanish government AEI for the financial support under Grants No. PID2023-148746OB-I00 and No. PID2023-146720OB-C21 (HEA4-COAT). The authors wish to thank Comunidad de Madrid and European Structural Funds for their financial support to ACES4NET0-CM project (TEC-2024/ECO-116). The authors also wish to thank Instituto de Tecnologías para la Sostenibilidad (ITPS) for funding through the synergistic projects program.

Data availability

No data was used for the research described in the article.

References

[1] S. Chen, G. Shi, Two-dimensional materials for halide perovskite-based optoelectronic devices, Adv. Mater. 29 (2017), https://doi.org/10.1002/adma.201605448.
[2] A. Ávila-López, J.C. Cruz, J.A. Díaz-Real, K. García-Uitz, D. Cante-Góngora, G. Rodríguez-May, A review of Perovskite-based solar cells over the last decade: the evolution of the hole transport layer and the use of WO3 as an electron transport layer, Coatings 15 (2025) 132, https://doi.org/10.3390/COATINGS15020132.
[3] S. Hu, H.J. Snaith, Solar cells that combine multiple perovskite layers surpass 30% efficiency, Nature 648 (2025), https://doi.org/10.1038/d41586-025-03806-x.
[4] J. Zhao, Y. Deng, H. Wei, X. Zheng, Z. Yu, Y. Shao, J.E. Shield, J. Huang, Strained hybrid perovskite thin films and their impact on the intrinsic stability of perovskite solar cells, Sci. Adv. 3 (2017), https://doi.org/10.1126/sciadv.aao5616.
[5] J. Han, S. Wei, X. Ren, L. Yu, L. Sun, S. Yue, W. Li, M. Wu, H. Qin, Bandgap prediction for perovskite materials based on symbolic-neural hybrid modeling, mater, Today Energy 54 (2025), https://doi.org/10.1016/j.mtener.2025.102075.
[6] P. Priyadarshini, S. Senapati, R. Naik, Lead-free organic inorganic hybrid halide perovskites: an emerging candidate for bifunctional applications, Renew. Sustain. Energy Rev. 186 (2023), https://doi.org/10.1016/j.rser.2023.113649.
[7] M. Aghaei, A. Fairbrother, A. Gok, S. Ahmad, S. Kazim, K. Lobato, G. Oreski, A. Reinders, J. Schmitz, M. Theelen, P. Yilmaz, J. Kettle, Review of degradation and failure phenomena in photovoltaic modules, Renew. Sustain. Energy Rev. 159 (2022), https://doi.org/10.1016/j.rser.2022.112160.
[8] M. Dailey, Y. Li, A.D. Printz, Residual film stresses in perovskite solar cells: origins, effects, and mitigation strategies, ACS Omega 6 (2021) 30214–30223, https://doi.org/10.1021/ACSOMEGA.1C04814.
[9] B. Nath, A. Panchal, J. Kumar, B. Singh, S.C. K, S.R. Rondiya, P.C. Ramamurthy, Low-temperature-processed flexible perovskite solar cells: performance analysis and stability dynamics, ACS Appl. Energy Mater. 8 (2025) 17297–17310, https://doi.org/10.1021/ACSAEM.5C02466.
[10] S. Mahalingam, A. Manap, D. Floresyona, R. Rabeya, N. Afandi, Z. Hasan, A. Nugroho, Advancements in flexible perovskite solar cells enabling self-powered systems, Renew. Sustain. Energy Rev. 213 (2025), https://doi.org/10.1016/j.rser.2025.115488.
[11] B. Li, Y. Yao, C. Kan, P. Hang, J. Xie, Q. Yin, D. Zhang, X. Yu, D. Yang, Promising excitonic absorption for efficient perovskite solar cells, Joule 9 (2025) 101780, https://doi.org/10.1016/j.joule.2024.10.012.
[12] S. Rabhi, K. Sekar, K. Kalna, Y.I. Bouderbala, N. Bouri, N. Oueldna, N. Belbachir, K. Dadda, M.S. Aida, N. Attaf, Experimental findings and SCAPS-1D simulations for high-efficiency MAPbI3 perovskite solar cells beyond 31%, Opt. Quant. Electron. 56 (2024) https://doi.org/10.1007/S11082-024-07282-X.
[13] C. Son, H. Son, B.S. Jeong, Enhanced conversion efficiency in MAPbI3 perovskite solar cells through parameters optimization via SCAPS-1D simulation, Appl. Sci. 14 (2024) 2390, https://doi.org/10.3390/APP14062390, 2390 14 (2024.
[14] N. Rolston, A.D. Printz, J.M. Tracy, R.H. Dauskardt, Effect of composition and microstructure on the mechanical stability of perovskite solar cells. 2018 IEEE 7th World Conference on Photovoltaic Energy Conversion, WCPEC 2018 - a Joint Conference of 45th IEEE PVSC, 28th PVSEC and 34th, EU PVSEC, 2018, pp. 3509–3513, https://doi.org/10.1109/PVSC.2018.8547641.
[15] C.M. Magazzeni, H.M. Gardner, I. Howe, P. Gopon, J.C. Waite, D. Rugg, D.E. J. Armstrong, A.J. Wilkinson, Nanoindentation in multi-modal map combinations: a correlative approach to local mechanical property assessment, J. Mater. Res. 36 (2021) 2235–2250, https://doi.org/10.1557/S43578-020-00035-Y.
[16] J. Li, C. Ge, Z. Zhao, M. Hu, J. Wang, F. Qian, X. Chong, J. Feng, Mechanical properties of single crystal organic–inorganic hybrid Perovskite MAPbX3 (MA = CH3NH3, X = Cl, Br, I), Coatings 13 (2023) 854–868, https://doi.org/10.3390/COATINGS13050854.
[17] Z. Dai, M.C. Doyle, X. Liu, M. Hu, Q. Wang, C.E. Athanasiou, Y. Liu, B.W. Sheldon, H. Gao, S. Frank, Liu, N.P. Padture, The mechanical behavior of metal-halide perovskites: elasticity, plasticity, fracture, and creep, Scr. Mater. 223 (2023), https://doi.org/10.1016/j.scriptamat.2022.115064.
[18] S. Baumann, G.E. Eperon, A. Virtuani, Q. Jeangros, D.B. Kern, D. Barrit, J. Schall, W. Nie, G. Oreski, M. Khenkin, C. Ulbrich, R. Peibst, J.S. Stein, M. Köntges, Stability and reliability of perovskite containing solar cells and modules: degradation mechanisms and mitigation strategies, Energy Environ. Sci. 17 (2024) 7566–7599, https://doi.org/10.1039/D4EE01898B.
[19] S. Kumar, S.S. Sharma, J. Giri, E. Makki, T. Sathish, H. Panchal, Perovskite materials with improved stability and environmental friendliness for photovoltaics, Front. Mech. Eng. 10 (2024) 1357087, https://doi.org/10.3389/FMECH.2024.1357087.
[20] R. Janisch, D. Mordehai, The nanoindentation puzzle: putting the pieces together using simulations at different scales, MRS Bull. 50 (6) (2025) 749–762, https://doi.org/10.1557/S43577-025-00920-Z, 50 (2025.
[21] Y. Yang, R. Chen, M. Yang, L. Xi, Z. Chen, Z. Yang, G. Zhang, C. Qin, J. Hu, L. Xiao, S. Jia, Impact of hexagonal boron Nitride encapsulation on the photophysical dynamics of MAPbI3 perovskite crystals, J. Phys. Chem. Lett. 16 (2025) 2972–2980, https://doi.org/10.1021/ACS.JPCLETT.4C03715.
[22] M.J. Namvar, M.H. Abbaspour-Fard, M. Rezaee Roknabadi, A. Behjat, M. Mirzaei, Enhancement of perovskite solar cells characteristics by incorporating mixed sodium/cesium cations, Optik (Stuttg) 185 (2019) 1019–1023, https://doi.org/10.1016/J.IJLEO.2019.04.052.
[23] R.A. Afre, D. Pugliese, Perovskite solar cells: a review of the latest advances in materials, fabrication techniques, and stability enhancement strategies, Micromachines (Basel) 15 (2024) 192, https://doi.org/10.3390/MI15020192.
[24] N. Rolston, A.D. Printz, J.M. Tracy, H.C. Weerasinghe, D. Vak, L.J. Haur, A. Priyadarshi, N. Mathews, D.J. Slotcavage, M.D. McGehee, R.E. Kalan, K. Zielinski, R.L. Grimm, H. Tsai, W. Nie, A.D. Mohite, S. Gholipour, M. Saliba, M. Grätzel, R.H. Dauskardt, Effect of cation composition on the mechanical stability of perovskite solar cells, Adv. Energy Mater. 8 (2018) 1702116, https://doi.org/10.1002/AENM.201702116.
[25] M.C. López-González, G. del Pozo, B. Arredondo, S. Delgado, D. Martín-Martín, M. García-Pardo, B. Romero, Temperature behaviour of mixed-cation mixed-halide perovskite solar cells. Analysis of recombination mechanisms and ion migration, Org. Electron. 120 (2023) 106843, https://doi.org/10.1016/J.ORGEL.2023.106843.
[26] C. Eames, J.M. Frost, P.R.F. Barnes, B.C. O'Regan, A. Walsh, M.S. Islam, Ionic transport in hybrid lead iodide perovskite solar cells, Nat. Commun. 6 (2015) 7497, https://doi.org/10.1038/ncomms8497.
[27] J.M. Azpiroz, E. Mosconi, J. Bisquert, F. De Angelis, Defect migration in methylammonium lead iodide and its role in perovskite solar cell operation, Energy Environ. Sci. 8 (2015) 2118–2127, https://doi.org/10.1039/C5EE01265A.
[28] L. Contreras-Bernal, S. Ramos-Terrón, A. Riquelme, P.P. Boix, J. Idígoras, I. Mora-Seró, J.A. Anta, Impedance analysis of perovskite solar cells: a case study, J. Mater. Chem. A Mater 7 (2019) 12191–12200, https://doi.org/10.1039/C9TA02808K.
[29] V. Maier-Kiener, S.K. Lawrence, B. Merle, 30 years of Oliver–Pharr: then, now and the future of nanoindentation, JOM 74 (2022) 2177–2178, https://doi.org/10.1007/S11837-022-05305-0.
[30] W.C. Oliver, G.M. Pharr, An improved technique for determining hardness and elastic modulus using load and displacement sensing indentation experiments, J. Mater. Res. 7 (1992) 1564–1583, https://doi.org/10.1557/JMR.1992.1564.
[31] J. Hay, P. Agee, E. Herbert, Continuous stiffness measurement during instrumented indentation testing, Exp. Tech. 34 (2010) 86–94, https://doi.org/10.1111/J.1747-1567.2010.00618.X.
[32] P.S. Phani, W.C. Oliver, G.M. Pharr, On the effective load during nanoindentation creep testing with continuous stiffness measurement (CSM), J. Mater. Res. 36 (2021) 1740–1750, https://doi.org/10.1557/S43578-021-00235-0.
[33] F.J. Ulm, M. Vandamme, C. Bobko, J. Alberto Ortega, K. Tai, C. Ortiz, Statistical indentation techniques for hydrated nanocomposites: concrete, bone, and shale, J. Am. Ceram. Soc. 90 (2007) 2677–2692, https://doi.org/10.1111/J.1551-2916.2007.02012.X.
[34] A. Chorfa, A. Madjoubi Mohamed Mohamed, M. Hamidouche, N. Bouras, J. Rubio, F. Rubio, Glass hardness and elastic modulus determination by nanoindentation using displacement and energy methods, Ceramics – Silikáty 54 (2010) 225–234. https://www.ceramics-silikaty.cz/index.php?page=cs_detail_doi&id=366. (Accessed 4 May 2026).
[35] I. Buchine, I. Rosenhek-Goldian, N.P. Jasti, D.R. Ceratti, S. Kumar, D. Cahen, S. R. Cohen, Nanomechanical signatures of degradation-free influence of water on halide perovskite mechanics, Commun. Mater. 3 (2022) 70, https://doi.org/10.1038/s43246-022-00287-7.
[36] Y. Rakita, S.R. Cohen, N.K. Kedem, G. Hodes, D. Cahen, Mechanical properties of APbX3 (A=Cs or CH3NH3; X=I or Br) perovskite single crystals, MRS Commun. 5 (2015) 623–629, https://doi.org/10.1557/mrc.2015.69.
[37] S. Seong, S. Seong, Y. Liu, Y. Liu, X. Gong, X. Gong, X. Gong, X. Gong, X. Gong, Mechanical study of perovskite solar cells: opportunities and challenges for wearable power source, Opt. Mater. Express 12 (2022) 772–787, https://doi.org/10.1364/OME.450214.
[38] C. Ramirez, S.K. Yadavalli, H.F. Garces, Y. Zhou, N.P. Padture, Thermo-mechanical behavior of organic-inorganic halide perovskites for solar cells, Scr. Mater. 150 (2018) 36–41, https://doi.org/10.1016/J.SCRIPTAMAT.2018.02.022.
[39] M. Spina, A. Karimi, W. Andreoni, C.A. Pignedoli, B. Náfrádi, L. Forró, E. Horváth, Mechanical signatures of degradation of the photovoltaic perovskite CH3NH3PbI3

upon water vapor exposure, Appl. Phys. Lett. 110 (2017) 121903, https://doi.org/10.1063/1.4978687/33210.
[40] S. Sun, Y. Fang, G. Kieslich, T.J. White, A.K. Cheetham, Mechanical properties of organic–inorganic halide perovskites, CH3NH3PbX3 (X = I, Br and Cl), by nanoindentation, J. Mater. Chem. A Mater. 3 (2015) 18450–18455, https://doi.org/10.1039/C5TA03331D.
[41] J. Feng, Mechanical properties of hybrid organic-inorganic CH3NH 3BX3 (B = Sn, Pb; X = Br, I) perovskites for solar cell absorbers, APL Mater. 2 (2014) 81801, https://doi.org/10.1063/1.4885256/120752.
[42] Z. Dai, M.C. Doyle, X. Liu, M. Hu, Q. Wang, C.E. Athanasiou, Y. Liu, B.W. Sheldon, H. Gao, S. Frank, Liu, N.P. Padture, The mechanical behavior of metal-halide perovskites: elasticity, plasticity, fracture, and creep, Scr. Mater. 223 (2023) 115064, https://doi.org/10.1016/J.SCRIPTAMAT.2022.115064.
[43] M. Faghihnasiri, M. Izadifard, M.E. Ghazi, DFT study of mechanical properties and stability of cubic methylammonium lead halide perovskites (CH3NH3PbX3, X = I, Br, cl), J. Phys. Chem. C 121 (2017) 27059–27070, https://doi.org/10.1021/ACS.JPCC.7B07129.
[44] W.W. Liu, C.X. Li, C.Y. Cui, G.L. Liu, Y.X. Lei, Y.W. Zheng, S.J. Da, Z.Q. Xu, R. Zou, L. Bin Kong, F. Ran, Strengthened interficial adhesive fracture energy by young's modulus matching degree strategy in carbon-based HTM free MAPbI3 perovskite solar cell with enhanced mechanical compatibility, Small 20 (2024), https://doi.org/10.1002/SMLL.202304452.
[45] Y. He, X. Miao, W. Wang, J. Li, J. Zhang, R. Li, L. Yang, L. Liu, Y. Wang, Z. Guo, D. Zhao, K. Lan, High-volumetric pseudocapacitive sodium storage in densely packed mesoporous titanium dioxide-carbon composite, Cell Rep. Phys. Sci. 5 (2024) 102123, https://doi.org/10.1016/J.XCRP.2024.102123.
[46] F. Roncaroli, E.D. Martínez, G.J.A.A. Soler-Illia, M.A. Blesa, Mesoporous thin films of TiO2 on attenuated total reflection crystals. An in situ fourier-transform infrared study of the kinetics and equilibrium of adsorption and photocatalysis of carboxylic acids, J. Phys. Chem. C 117 (2013) 15026–15034, https://doi.org/10.1021/JP312334Y.
[47] O. Anderson, C.R. Ottermann, R. Kuschnereit, P. Hess, K. Bange, Density and Young's modulus of thin TiO2 films, Fresenius J. Anal. Chem. 358 (1997) 315–318, https://doi.org/10.1007/S002160050416.
[48] C.R. Ottermann, R. Kuschnereit, O. Anderson, P. Hess, K. Bange, Young's modulus and density of thin TiO2 films produced by different methods, MRS Online Proc. Libr. 436 (1) (1997) 251–256, https://doi.org/10.1557/PROC-436-251, 436 (2011.
[49] N. Haddad, M. Nouiri, Z. Ben Ayadi, A comprehensive investigation of structural and electrical characteristics of fluorine-doped tin oxide nanoparticles for future optoelectronic applications, J. Electron. Mater. 53 (2024) 6181–6194, https://doi.org/10.1007/S11664-024-11279-3.
[50] L.T.C. Tuyen, S.R. Jian, N.T. Tien, P.H. Le, Nanomechanical and material properties of fluorine-doped tin oxide thin films prepared by ultrasonic spray pyrolysis: effects of F-Doping, Materials 12 (2019) 1665, https://doi.org/10.3390/MA12101665.
[51] M.A. Reyes-Martinez, A.L. Abdelhady, M.I. Saidaminov, D.Y. Chung, O.M. Bakr, M. G. Kanatzidis, W.O. Soboyejo, Y.L. Loo, Time-Dependent mechanical response of APbX3 (A = Cs, CH3NH3; X = I, Br) single crystals, Adv. Mater. 29 (2017) 1606556, https://doi.org/10.1002/ADMA.201606556.
[52] R. Chen, L. Lang, M. Xie, J. Pang, N. Qu, Y. Zou, Probing mechanical properties of various halide perovskites by nanoindentation, MRS Commun. 15 (2025) 796–802, https://doi.org/10.1557/S43579-025-00763-4.
[53] D.F. Lionello, J.I. Ramallo, G.J.A.A. Soler-Illia, M.C. Fuertes, Mechanical properties of ordered mesoporous oxides thin films, J. Sol. Gel Sci. Technol. 101 (1) (2021) 114–139, https://doi.org/10.1007/S10971-021-05626-7, 101 (2021.
[54] D. Kaczmarek, J. Domaradzki, D. Wojcieszak, E. Prociow, M. Mazur, F. Placido, S. Lapp, Hardness of nanocrystalline TiO2 thin films, J. Nano Res. 18–19 (2012) 195–200, https://doi.org/10.4028/WWW.SCIENTIFIC.NET/JNANOR.18-19.195.
[55] A. Wiatrowski, M. Mazur, A. Obstarczyk, D. Wojcieszak, D. Kaczmarek, J. Morgiel, D. Gibson, Comparison of the physicochemical properties of TiO2 thin films obtained by magnetron sputtering with continuous and pulsed gas flow, Coatings 8 (2018) 412, https://doi.org/10.3390/COATINGS8110412, 412 8 (2018.
[56] S. Zak, C.O.W. Trost, P. Kreiml, M.J. Cordill, Accurate measurement of thin film mechanical properties using nanoindentation, J. Mater. Res. 37 (7) (2022) 1373–1389, https://doi.org/10.1557/S43578-022-00541-1, 37 (2022.
[57] D. Reynolds, Gaussian mixture models, Encyclopedia Biometr. (2009) 659–663, https://doi.org/10.1007/978-0-387-73003-5_196.